

# Electrosynthesis of Iron-Based Metal–Organic Materials with Bis(salicylic acid) Derivatives

Sara Realista,<sup>\*,#</sup> Ana R. Reis,<sup>#</sup> Duarte Borralho, Victoria Corregidor, Luís C. Alves, Sérgio Magalhães, Telmo Nunes, Ana S. Viana, João Pires, Ana M. Ferraria, Ana M. Botelho do Rego, and Paulo N. Martinho



Cite This: *J. Phys. Chem. C* 2024, 128, 11904–11914



Read Online

ACCESS |



Metrics & More

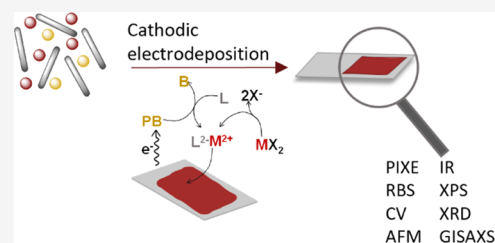


Article Recommendations



Supporting Information

**ABSTRACT:** This study examines the electrosynthesis of novel iron-organic films via cathodic electrodeposition using cyclic voltammetry to establish suitable deposition potentials for two different organic linkers: 2,5-dihydroxyterephthalic acid (DOBDC) and 3,3'-dihydroxybiphenyl-4,4'-dicarboxylic acid (BPP). The synthesis process focuses on the coordination of carboxylate to iron centers, producing amorphous films. Analytical techniques including infrared spectroscopy, scanning electron microscopy, X-ray photoelectron spectroscopy, atomic force microscopy (AFM), and a combination of particle-induced X-ray emission and Rutherford backscattering spectrometry were employed to characterize the films' chemical, morphological, and structural properties. AFM analysis highlighted the evolution of film morphology with deposition time, revealing a transition from highly ordered to more random structures, influencing film crystallinity. Electrochemical assessments demonstrated the stability and electroactive nature of the films, with their behavior dependent on the specific linker used, reflected in the varied electrochemical responses and film properties observed. The study not only refines the synthesis process for metal–organic films but also delineates the impact of synthesis parameters such as linker type, deposition time, and applied potential on the properties of the resulting materials, paving the way for future investigations into diverse electrosynthesis conditions and deprotonation mechanisms for creating innovative metal–organic materials.



## INTRODUCTION

New functionalized surfaces are crucial for the development of materials science, as they enable the exploration of novel properties and functionalities, expand the range of applications for materials, and drive innovation in different industries. By continually advancing the understanding and control of surface properties, materials scientists can unlock new possibilities for designing materials with tailored characteristics, improved performance, and enhanced functionality, thereby pushing the boundaries of scientific knowledge and technological development.<sup>1–3</sup> The newly designed materials can have new or improved properties, such as conductivity, reactivity, photoactivity, and catalytic performance.<sup>2</sup>

There are several physical and chemical methods for the formation of thin films based on inorganic and/or organic compounds such as atomic layer deposition, sputtering, chemical vapor deposition, metal–organic chemical vapor deposition, molecular beam epitaxy, electrodeposition, and spin-coating, among others.<sup>4</sup> Many candidates have been used for deposition as metal oxides,<sup>5</sup> nanoparticles,<sup>6,7</sup> polymers,<sup>8,9</sup> and metal alloys,<sup>10</sup> and among them, metal–organic materials (MOMs) started to attract attention due to their outstanding film-forming properties, diverse metal centers and ligand sources, and the ability to design both their structure and function.<sup>11,12</sup> MOMs are built from the self-assembly of metal

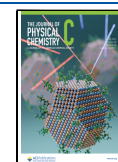
ions (nodes) and organic ligands (linkers) and are exemplified by a vast group of discrete (e.g., metal–organic polyhedra, spheres or nanoballs, and metal–organic polygons) or polymeric structures (e.g., porous coordination polymers, PCPs, metal–organic frameworks, MOFs, or hybrid inorganic–organic materials).<sup>13</sup> Presently, there is growing attention on broadening materials that are commonly identified as CPs<sup>14</sup> or MOFs,<sup>15</sup> with the latter designation applying to structures that are crystalline and feature high porosity. While MOF films have their benefits, MOM films offer some exclusive features, particularly for practical implementations. MOM films could be either amorphous or crystalline in structure, and therefore, they are more structurally flexible than dominantly crystalline MOFs. Films based on MOM show enhanced mechanical flexibility and robustness and thus are found to be suitable for wearable sensors and flexible electronics. They can incorporate mixed-valence metal centers that enhance electrical conduction and

Received: April 23, 2024

Revised: June 21, 2024

Accepted: June 21, 2024

Published: July 8, 2024



electrochemical activity. They also produce continuous, homogeneous coatings, which are crucial for protective coatings, sensors, and catalysis, whereas MOF films often face challenges in achieving such continuity due to their rigid and porous structure.<sup>16,17</sup>

Although MOMs date back to the 1950s, interest in supramolecular metal–organic thin films is escalating due to their extensive selection of components, hybrid physicochemical characteristics, and adaptable reactivity.<sup>1,18–22</sup> Moreover, understanding the self-assembly mechanisms enables precise manipulation of the structural and functional features of the films.<sup>23</sup> Their structural and chemical versatility continues to fuel scientific intrigue and technological advancements, paving the way for customization in several applications from gas management and separation to advancements in sensing, catalysis, photonics, electronics, and energy solutions.<sup>11,24</sup>

Here we report the synthesis of two new MOM-based films using the cathodic electrodeposition method (Figure 1a) that

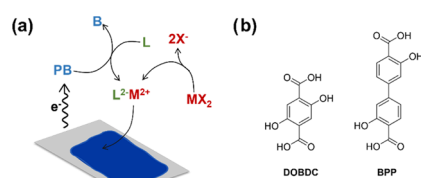


**Figure 1.** (a) Mechanism of the cathodic deposition of MOMs (PB = probase, B = base, M = metal node, L = organic linker); (b) linkers used in this study.

allows us to have shorter synthesis times under milder conditions and the ability to fine-tune morphology as key advantages.<sup>25</sup> When compared with the anodic dissolution method, it gives the possibility of using nonmetal electrode substrates and different metal ions. This method has not been yet explored for a wide range of metal ions and linkers, which gives a great opportunity to develop the state-of-the-art method by solidly developing a transferable methodology for the highly controlled synthesis of MOM films. Two distinct organic linkers (Figure 1b) were selected to investigate the effect of the linker length, namely 2,5-dihydroxyterephthalic acid (DOBDC) and 3,3'-dihydroxybiphenyl-4,4'-dicarboxylic acid (BPP).  $\text{FeCl}_3 \cdot 6\text{H}_2\text{O}$  was used as the metal salt for providing iron as the metal node for the MOM film, since upon electroreduction, a possible mixed-valence state could potentially boost the conductivity.<sup>26</sup> With this, it is reasonable to assert that an elevated understanding of the molecular processes at interfaces will enhance the knowledge of the research field in order to build new and improved functional interfaces.

## MATERIALS AND METHODS

**General Procedures.** If not stated otherwise, all chemicals were used without further purification and purchased from TCI, Sigma-Aldrich, Fluorochem, and Acros Organics. BPP was synthesized according to the literature.<sup>27</sup> When indicated, solvents were purified as described by Armarego and Perrin.<sup>28</sup>  $^1\text{H}$  and  $^{13}\text{C}$  NMR spectra were recorded on a Bruker Avance 400 MHz spectrometer.

**Electrochemical Experiments.** Generally, a potentiostat PGSTAT 12 AUT71019 controlled by NOVA 2.0 software was used. For all of the experiments, a three-electrode electrochemical heart-shaped glass cell was used. As for the

electrodes, a platinum wire was used as a counter electrode and  $\text{Ag}/\text{AgCl}$ , 3 M  $\text{NaCl}$  (0.278 V vs NHE) as a reference electrode. The working electrode was a fluorine tin oxide (FTO) electrode with an area of  $0.7 \text{ cm}^2$ . FTO electrodes were ultrasonically washed before experiments with a detergent/water solution, methanol, and acetone for 15 min with each solution. Before any electrochemical measurements, the cell solutions were purged by bubbling  $\text{N}_2$  for a minimum of 30 min. 0.1 M of tetrabutylammonium hexafluorophosphate ( $\text{TBAPF}_6$ ) was used as the supporting electrolyte, which was previously recrystallized from hot ethanol.

Both cyclic voltammetry (CV) and chronoamperometry experiments were performed under an organic medium with 10 mL of dimethylformamide (DMF) and 0.1 M  $\text{TBAPF}_6$  with or without other components. For the deposition on the films, the precursor solution was constituted by the metal ion ( $\text{M} = \text{FeCl}_3 \cdot 6\text{H}_2\text{O}$ ), the proligand (PL = DOBDC or BPP), and the probase (PB =  $\text{Et}_3\text{NHCl}$ ) in a ratio of 2:1:1 (M:PL:PB, respectively). One-step electrodeposition was performed by applying  $-1.4$ ,  $-1.3$ , or  $-1.2$  V vs reference electrode for 1 h. After the deposition, the electrode was dried at room temperature and washed with DMF and acetone.

The films were studied for their redox and voltammetric behavior in DMF solution containing 0.1 M  $\text{TBAPF}_6$  with or without 1 mM of ferrocene.

**Physical Characterizations.** Scanning electron microscopic (SEM) images were obtained by means of a JEOL JSM-5200LV scanning electron microscope. Previously, the films were mounted in stubs and coated with gold in a JEOL JFC-1200 sputtering chamber.

Powder X-ray diffractograms (XRD) were acquired using a Philips Analytical PW 3050/60 X'Pert PRO automatic diffractometer ( $\theta/2\theta$ ), equipped with an X'Celerator detector, with automatic data acquisition using the X'Pert Data Collector software, version 2.0b. As incident radiation, the  $K\alpha$  line of a copper bulb was used, operating with a current of 30 mA and a voltage of 40 kV. To record the diffractograms, a continuous scan of the Bragg angles was performed, for values of  $2\theta$ , between 10 and  $90^\circ$ , with a step of  $0.017^\circ$  ( $2\theta$ ) and an acquisition time of 20 s/step. The grazing-incidence small-angle X-ray scattering (GISAXS) spectra were acquired using a Bruker D8 AXS diffractometer equipped with a Cu source. To limit the vertical divergence, a Göbel mirror and a Söller slit were used in the primary and secondary beam paths, respectively. The measurements were performed with a  $2\theta$  step of  $0.01^\circ$  ranging from  $-20$  to  $20^\circ$  and an  $\alpha$  step of  $1^\circ$  from 0 to  $2^\circ$ . The accumulation time is set to 1 s/step. The system operated at 40 mA/40 kV. The diffracted/reflected counts per second were registered in proprietary software (Commander) using a point focus detector.

For PIXE (particle-induced X-ray emission) and RBS (Rutherford backscattering spectrometry) techniques, a 2 MeV proton beam generated by a 2.5 MV single-ended Van de Graaff accelerator and directed to the microprobe beamline through a  $90^\circ$  bending magnet was utilized. The nuclear microprobe has an Oxford Microbeams magnetic quadrupole triplet used to focus the beam up to  $3 \times 4 \mu\text{m}^2$ .<sup>29</sup> The measurements are performed under vacuum conditions, and the experimental chamber has a  $30 \text{ mm}^2$  Bruker Si SDD detector with  $8 \mu\text{m}$  Be window and 145 eV resolution at 5.9 keV, positioned at  $135^\circ$  with the beam direction at a distance of 20 mm from the sample, used to record the PIXE spectra. The backscattered protons are detected with a  $200 \text{ mm}^2$  PIPS

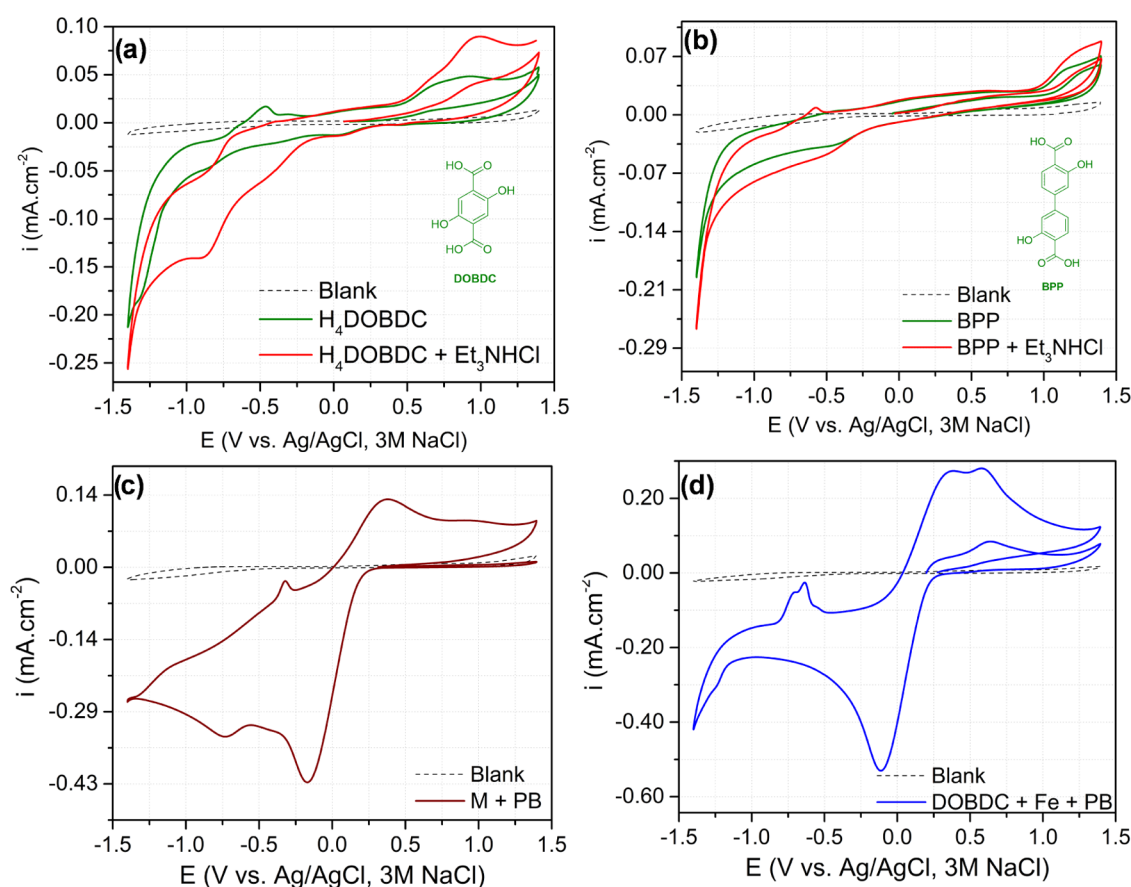


**Figure 2.** Cyclic voltammograms of (a) DOBDC and (b) BPP (2 mM) with and without Et<sub>3</sub>NHCl (2 mM). Cyclic voltammograms of (c) a mixture of FeCl<sub>3</sub>·6H<sub>2</sub>O (4 mM) and PB (2 mM) and (d) after DOBDC (2 mM) is added in 0.1 M TBAPF<sub>6</sub>/DMF solutions under N<sub>2</sub> atmosphere at 100 mV s<sup>-1</sup>. 0.1 M TBAPF<sub>6</sub> (0.1 M) was used as a supporting electrolyte.

detector with 30 keV resolution, positioned at a 140° scattering angle in Cornell geometry at a 50 mm distance from the sample. Operation and basic data manipulation, including elemental distribution mapping, was achieved through the OMDAQ software code. Quantitative PIXE spectra analysis is done with GUPIX software<sup>30</sup> and the results are expressed in weight percent normalized to 100%. Furthermore, NDF v9.6a code simultaneously fits the PIXE and RBS spectra to obtain a self-consistent solution.<sup>31</sup> Thickness values are obtained in areal density (i.e., atoms/cm<sup>2</sup>), the standard units in IBA analyses, and they were converted into nanometer units considering the areal density and molecular mass of the compounds. The RBS fits consider the double scattering contribution and the pulse pile-up effect. The non-Rutherford cross-sections for C, O, and Si were included in the fitting model,<sup>32</sup> as well as the roughness of the surface using the  $\gamma$  roughness algorithm.<sup>33</sup>

X-ray photoelectron spectroscopy (XPS) analyses were performed with a dual anode (Al/Mg) nonmonochromatic spectrometer XSAM800 from KRATOS. The X-radiation Mg K $\alpha$  ( $h\nu = 1253.6$  eV) used to irradiate the samples was produced with a high voltage of 12 kV and filaments current equal to 10 mA. Samples were fixed to the XPS holder with a metal spring and positioned in the analysis chamber at a takeoff angle of 90° relative to the surface. The analysis, at room temperature, started once the chamber attained an ultrahigh vacuum (UHV), typically a pressure of  $\sim 10^{-9}$  mbar. Spectra were acquired in a fixed analyzer transmission (FAT) mode,

with a pass energy of 20 eV, and collected and stored in 300 to 400 channels with a step of 0.1 eV using the software Vision 2 for Windows, Version 2.2.9 (Kratos). No flood gun was used to compensate for charge accumulation. Charge shift was corrected from the spectra using as reference the binding energy (BE) of aliphatic carbon bonded to carbon and/or hydrogen, set at 285 eV. Source satellites and Shirley backgrounds were subtracted at each region of interest. Component peaks with pseudo-Voigt profiles were fitted in each region with a nonlinear least-squares algorithm using the XPSPeak 4.1 software (freeware), which allows to optimize simultaneously peak position, area, full width at half-maximum, and percentage of Gaussian–Lorentzian components. The only constraints imposed were (i) for all the components, within a given region, identical full width at half-maximum (fwhm), and identical Lorentzian percentage; (ii) for the peaks corresponding to carbon bonded to oxygen atoms (second and third components), identical areas. The sensitivity factors used in the quantification were the following: C 1s: 0.318; O 1s: 0.736; N 1s: 0.505; Fe 2p<sub>3/2</sub>: 1.965; Cl 2p: 0.964; P 2p: 0.530; P 2s: 0.344; F 1s: 1.000; Sn 3d<sub>5/2</sub>: 4.946; Na 1s: 1.378.

Powder infrared spectra (IR) were obtained using a Nicolet Nexus 6700 FTIR spectrophotometer in the 4000–400 cm<sup>-1</sup> range with 4 cm<sup>-1</sup> resolution using KBr pellets with 64 scans. Film's IR spectra were obtained with the same spectrophotometer with the diffuse reflectance accessory in the 4000–750 cm<sup>-1</sup> range with 4 cm<sup>-1</sup> resolution and 256 scans.

AFM *ex situ* images were collected in a multimode atomic force microscope running on a NanoScope V controller (digital instrument Veeco) using PeakForce Tapping and ScanAsyst modes. The images were acquired at a scan rate of  $\approx 1.0$  Hz, using ScanAsyst-air probes (Bruker) with a spring constant of 0.4 N/m.

## RESULTS AND DISCUSSION

**Electrochemical Studies for Films' Electrosynthesis Optimization.** CV studies (Figure 2) on the precursors were performed to find the optimized potential to use for the potentiostatic growth of MOM films using two different linkers (Figure 1b, DOBDC and BPP). The studies were performed in DMF and using 0.1 M TBAPF<sub>6</sub> as the supporting electrolyte. FTO (a thin film of tin oxide-doped with fluorine on a glass substrate), platinum wire, and Ag/AgCl (3 M NaCl) were used as working, counter, and reference electrodes, respectively. Besides the metal ion source and the PL, a PB must be used for the cathodic electrodeposition to deprotonate the PL.<sup>34</sup> In contrast to other deposition methods, it enables the direct electrode surface deposition of a thin film, whereas postsolvothermal MOM powder synthesis needs an extra step for thin film deposition.

Et<sub>3</sub>NHCl was used as PB to perform the deposition because its reductive potential is more positive than other more commonly used PBs (e.g., H<sub>2</sub>O, NO<sub>3</sub><sup>-</sup>, O<sub>2</sub>), preventing metal deposition.<sup>35,36</sup> CV (Figure S1) of the PB shows its reduction to Et<sub>3</sub>N and H<sub>2</sub> at around -0.6 V vs Ag/AgCl (3 M NaCl) as reported in a 0.1 M TBAPF<sub>6</sub>/DMF solution.<sup>35,36</sup> When DOBDC is added to the PB solution (Figure 2a), a higher cathodic current density is observed, as an increase in proton concentration is expected, as previously observed by Li et al.<sup>36</sup> A similar behavior is observed when BPP is used (Figure 2b).

A solution containing FeCl<sub>3</sub>·6H<sub>2</sub>O (M) and PB (without the oPL) was also investigated (Figure 2c), and the CV shows that the PB influences the iron redox behavior (Figure S2a), as the reduction of Fe(II) to Fe(0) (above -1.2 V, Figure S2a) and the current density of its reoxidation to Fe(II) (-0.4 V, Figure S2b) substantially decreases. Therefore, the presence of the PB may prevent the undesirable deposition of Fe(0) at the FTO. When all the precursors for the film formation are present in the solution (M + PB + DOBDC or BPP, Figure 2d), the redox processes from the metal ion and the proligands are observed with an additional oxidation process at 0.60 V, which was also present when only the metal source and the proligand were mixed (Figure S2a). In addition, the process from the reoxidation of Fe(0) is substantially reduced. The results suggest the formation of a complex between M and DOBDC that will be further discussed in detail.

Attempts to deposit thin films with these precursors onto FTO involved applying different potentials (-1.2, -1.3, and -1.4 V) to the 0.1 M TBAPF<sub>6</sub> DMF solutions containing M, PB, and DOBDC or BPP, based on CV investigations to mitigate metal deposition. No film deposition occurred when -1.2 V was applied to the electrolyte containing DOBDC, while it occurred when DOBDC was replaced by BPP. Therefore, -1.3 and -1.4 V were used for DOBDC and -1.2 and -1.3 V for BPP (Figures S3–S4). The steady-state current density for the electrodeposition (Figures S3–S4) reached values in the range of -90 to -220  $\mu\text{A cm}^{-2}$  for all cases.

**Films' Chemical and Morphological Characterization.** *Infrared spectroscopy.* Under the cathodic deposition conditions discussed above, new films were formed on the

FTO surface (Figures 3 and S5) that were analyzed by IR. Figures 3 and S5a display the comparison between the IR

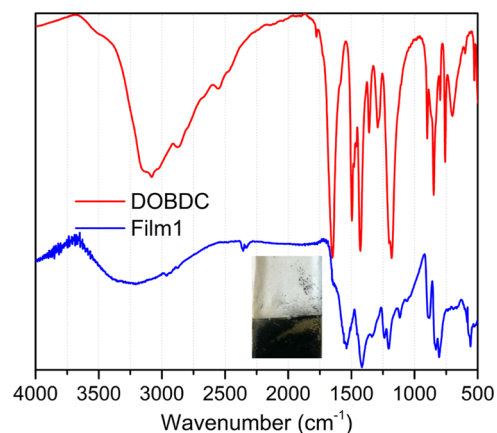


**Figure 3.** IR spectra of DOBDC (red) and Film1 (blue) formed by cathodic electrodeposition at -1.3 V vs Ag/AgCl (3 M NaCl). Inset: Picture of the film on the electrode.

spectra of the PL and the films grown at -1.3 V (Film1 for DOBDC and Film2 for BPP). No significant difference was observed between the spectra of the films grown at the other potentials used for each case. The IR spectrum of DOBDC shows the typical bands at 3520  $\text{cm}^{-1}$  ( $\nu_{\text{O-H,phenol}}$ ), 3082  $\text{cm}^{-1}$  ( $\nu_{\text{O-H,acid}}$ ), 3024  $\text{cm}^{-1}$  ( $\nu_{\text{C-H,aromatic}}$ ), 1646  $\text{cm}^{-1}$  ( $\nu_{\text{C=O}}$ ), 1427  $\text{cm}^{-1}$  ( $\delta_{\text{C-O,acid}}$ ), 1357–1182  $\text{cm}^{-1}$  ( $\nu_{\text{C-O,acid/phenol}}$ ), and 782  $\text{cm}^{-1}$  ( $\delta_{\text{C-H,Bz out-of-plane}}$ )  $\text{cm}^{-1}$ . For Film1 as expected, the band at 3520  $\text{cm}^{-1}$  disappears and the band at 1646  $\text{cm}^{-1}$  gives rise to the asymmetric and symmetric stretching bands of the carboxylate groups at 1538 and 1417  $\text{cm}^{-1}$ . Coordination of the iron centers is suggested in both phenolate and carboxylate groups of the DOBDC ligand. The same is observed for BPP and Film2 (Figure S5a).

Before film deposition and after adding DOBDC to the DMF solution containing M, a color change was observed. The IR spectrum of the solid residue of this solution is shown in Figure S5b. The IR spectra of the residue and the film deposited are different (Figure S5b). Although the stretching bands of carboxylate groups are observed (1575 and 1413  $\text{cm}^{-1}$ ), the stretching band of phenoxyl (3419  $\text{cm}^{-1}$ ) is also observed. The result indicates that deprotonation of the carboxylic acid groups occurs immediately (eq 1, Supporting Information (SI)), whereas the phenoxyl is only deprotonated during cathodic electrodeposition (eqs 2 and 3, SI). In fact, the results agree with previous reported studies, which display exclusively carboxylate coordination.<sup>37–40</sup>

**Scanning Electron Microscopy.** The morphology of the films was observed by SEM (Figures 4 and S6). For both Film1 and Film2, islands of plate-like aggregates were imaged with a nonhomogeneous dispersion. A plate size of approximately 1  $\mu\text{m}$  constitutes the aggregates in Film1, whereas smaller particles (<1  $\mu\text{m}$ ) are observed for Film2. The distribution of the aggregates is different in both films; fewer empty areas are observed for Film2. A BET surface of approximately 1161  $\text{m}^2 \text{g}^{-1}$  was obtained for Film1.

**X-Ray Powder Diffraction and Grazing-Incidence Small-Angle X-Ray Scattering.** Both coatings, Film1 and Film2, are amorphous (or with very small grain sizes), as XRD patterns were observed in the conventional Bragg–Brentano geometry. Even when a temperature treatment (100 °C for 12 h followed

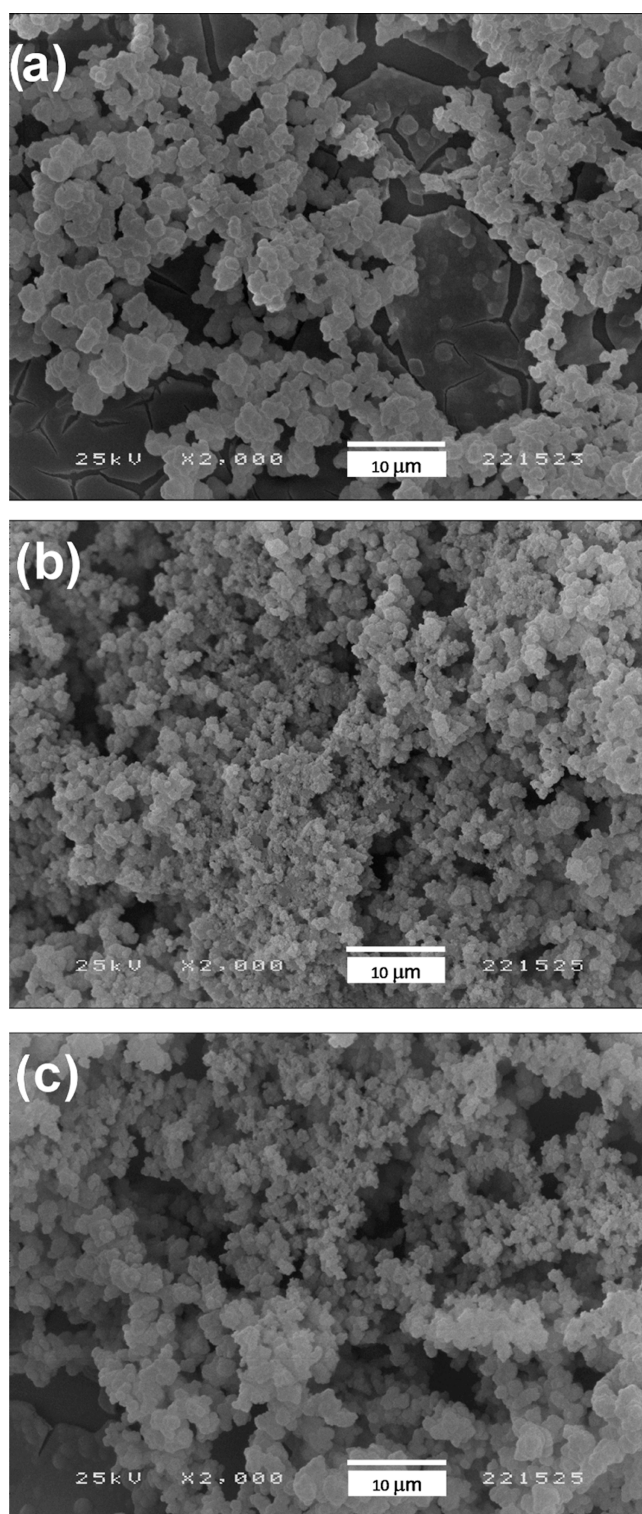


**Figure 4.** SEM images (x 2000) of (a) **Film1**, (b) **Film2**, and (c) **Film1-T** after temperature treatment (100 °C for 12 h followed by 200 °C for 2 h).

by 200 °C for 2 h)<sup>41</sup> labeled as **Film1-T** (Figure 4c) was performed in **Film1**, no XRD pattern was observed. The temperature treatment did not change the shape of the particles; however, larger islands were formed with a higher quantity of aggregates (Figure 4c).

To explore the (lack of) crystallinity, GISAXS were performed in **Film1** and **Film2** and compared to the ones

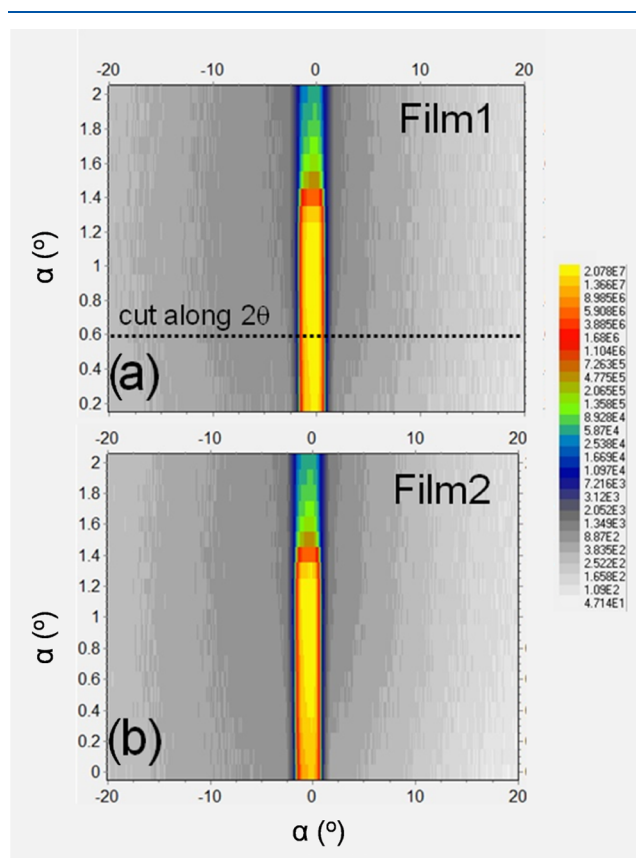


**Figure 5.** Maps of the GISAXS measurements acquired for samples (a) **Film1** and (b) **Film2**.

from the FTO and the glass substrates (Figures 5 and 6). GISAXS, as a surface-sensitive scattering technique, provides information on the nanoscale volumes deposited on surfaces,<sup>42</sup> e.g., the crystallinity of the aggregates, observed in Figure 4.

According to Figure 5a,b, at first glance, the two samples present similar GISAXS maps. Very similar maps were observed for the glass substrate and FTO (not shown). Using the mass density of Fe/C, a critical angle of 0.38°/0.22° is determined, whereas from the critical angle, a maximum penetration depth of 6.7 nm/8.8 nm is deduced. For  $\alpha < 0.38^\circ$ , the penetration depth is lower than that expected for the thickness of **Film1** and **Film2** (few hundreds of nanometres). Thus, no effect due to FTO is expected in the GISAXS measurements around the critical angle.

Figure 6 compares the individual cuts along  $2\theta$  for each  $\alpha$  of the GISAXS maps acquired for the FTO (a1–3), glass substrate (b1–3), and **Film1**/**Film2** (c/d1–3), respectively. Figure 6 (a<sub>2</sub>), (b<sub>2</sub>), and (c<sub>2</sub>) corresponds to the magnification along the intensity  $y$ -axis, while (a<sub>3</sub>), (b<sub>3</sub>), and (c<sub>3</sub>) are plotted by considering the  $2\theta$  axis between  $-15^\circ$  and  $10^\circ$ . A broad peak-like structure is present in the negative  $2\theta$  for **Film1** and **Film2**, while for the FTO and glass substrate, there is no clear diffraction. At the same time, **Film1** also exhibits a small peak for positive  $2\theta$  suggested to be due to very small grain sizes. The full width at half-maximum of the peaks observed for negative  $2\theta$  is highly inaccurate but can be estimated to be around  $10^\circ$ , which, according to the Scherrer formula, can correspond to grain sizes of around 1 nm.

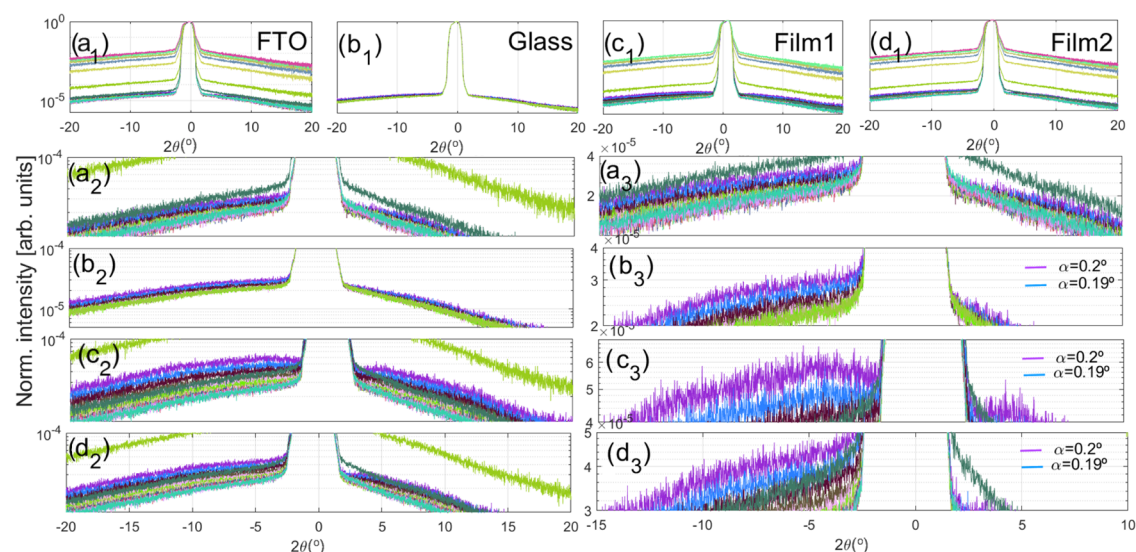


**Figure 6.** Maps of the GISAXS measurements acquired for samples (a) **Film1** and (b) **Film2**.

**X-Ray Photoelectron Spectroscopy.** The samples **Film1**, **Film2**, and **Film1**  $-1.4$  V were analyzed by XPS. In addition, a film grown from a solution at  $-1.3$  V without the proligand was obtained (**FilmFe**) and analyzed for comparison. In all the analyzed samples, the elements carbon, iron, oxygen, nitrogen, chlorine, and fluorine were detected. The detected fluorine has no counterpart of Sn in the major part of the samples; therefore, it cannot be assigned to the FTO substrate but rather to some electrolyte. The global quantification is gathered in [Table S1](#).

The detailed regions for Fe 2p, O 1s, and C 1s are shown in [Figure 7](#), and the corresponding data on fitted positions and atomic percent are presented in [Table S2](#).

C 1s region was fitted with three components: one set to 285 eV and used as a reference for the correction of binding energy shifts due to charge accumulation and assigned to carbon bonded to other carbon or hydrogen atoms; a second one ranging from 286.4 to 286.9 eV assigned to carbon bonded to oxygen through single bonds. For all the films, except **FilmFe** that is the one that was formed from a solution without the proligand, this component is due to phenolic groups in the ligands.<sup>43</sup> A third component was fitted at  $288.7 \pm 0.2$  eV and assigned to carboxylate groups. Therefore, the ligands have the carboxylic group mainly deprotonated.<sup>44</sup> For the **FilmFe**, the detected carbon is entirely assignable to the presence of a supporting electrolyte, probase, or solvent.

O 1s regions present a component at  $530.1 \pm 0.2$  eV, assignable to the lattice oxygen in iron oxides, for **FilmFe** and **Film1**  $-1.4$  V. It is not surprising that iron oxides are observed also for **Film1**  $-1.4$  V, as a more reductive potential will lead to higher iron deposition.<sup>35</sup> In **FilmFe**, as expected, it is the main component. Besides, also a component centered at 531.3 eV assignable, mainly to Fe–O–H groups is detected at the surface. The binding energies of **Film1** and **Film2** were fitted with two components at  $531.6 \pm 0.2$  eV assignable to the two equivalent oxygen atoms in the carboxylate group (O=C–O–) and another at  $532.5 \pm 0.2$  eV assigned to deprotonated phenolic oxygen, respectively (for protonated phenolic oxygen, O 1s binding energy should be 533.5 eV).<sup>43</sup> The same was obtained for **Film1**  $-1.4$  V spectrum, besides the above-referred peak at  $\sim 530$  eV. Moreover, qualitatively, the shape of

the iron region of these films is very similar to the shape found for **FilmFe** strongly suggesting that the oxidation state of iron in the complexes is Fe(III).

**Particle-Induced X-Ray Emission and Rutherford Backscattering Spectrometry.** As the films are heterogeneous, we decided to perform a surface and an in-depth characterization of both **Film1** and **Film2** using simultaneously PIXE and RBS techniques. 2D elemental distribution maps of Fe and Cl were obtained from the PIXE spectra and the Sn map from RBS spectra ([Figures 8](#) and [S7](#)). From the distribution maps, the films' surface heterogeneity is again revealed (cf. with SEM images). Also, while the Fe and Cl distributions are correlated, the Sn map (from the FTO electrode) shows an opposite correlation, with a higher Sn signal in the low film thickness zones indicating irregular film coverage with different thicknesses. Similar behavior was registered for **Film2** with different degrees of coverage. Point analyses ([Figure 8](#), red circles in the maps) allowed us to know the inorganic composition of the films from the PIXE spectra analysis, where only Fe, Cl, and P were detected as film constituents (Si, Ca, and Sn were also detected but attributed to the glass substrate and FTO layer).

For **Film1**, concentration values of Fe, Cl, and P in different points of the film ([Figure 8](#)) were 90, 3, and 5 wt %, respectively, while for **Film2** slightly different values were recorded, 88–89 wt % for Fe, 10 wt % for Cl, and less than <1 wt % for P. Besides the composition of the films, it was possible to estimate their thickness on the different points analyzed from the RBS spectra. While for **Film1**, the thickness values obtained are higher than 10  $\mu\text{m}$ , the thickness of **Film2** varies between 1.4 and 2.5  $\mu\text{m}$  ([Figure S7](#)), allowing also the detection of the presence of FTO and the glass substrate. An example of a PIXE and RBS spectra from **Film2** are shown in [Figure S8](#).

From the fit of the RBS spectra recorded in different points of the films, it was possible to obtain a depth profile for **Film1** and **Film2** ([Figure 9](#)). In both cases, it is possible to observe that there is more than one region where the same atom is found at a different concentration, highlighting the in-depth heterogeneity of these films. For **Film2**, it was possible to analyze all the in-depth profiles down to the FTO layer and the

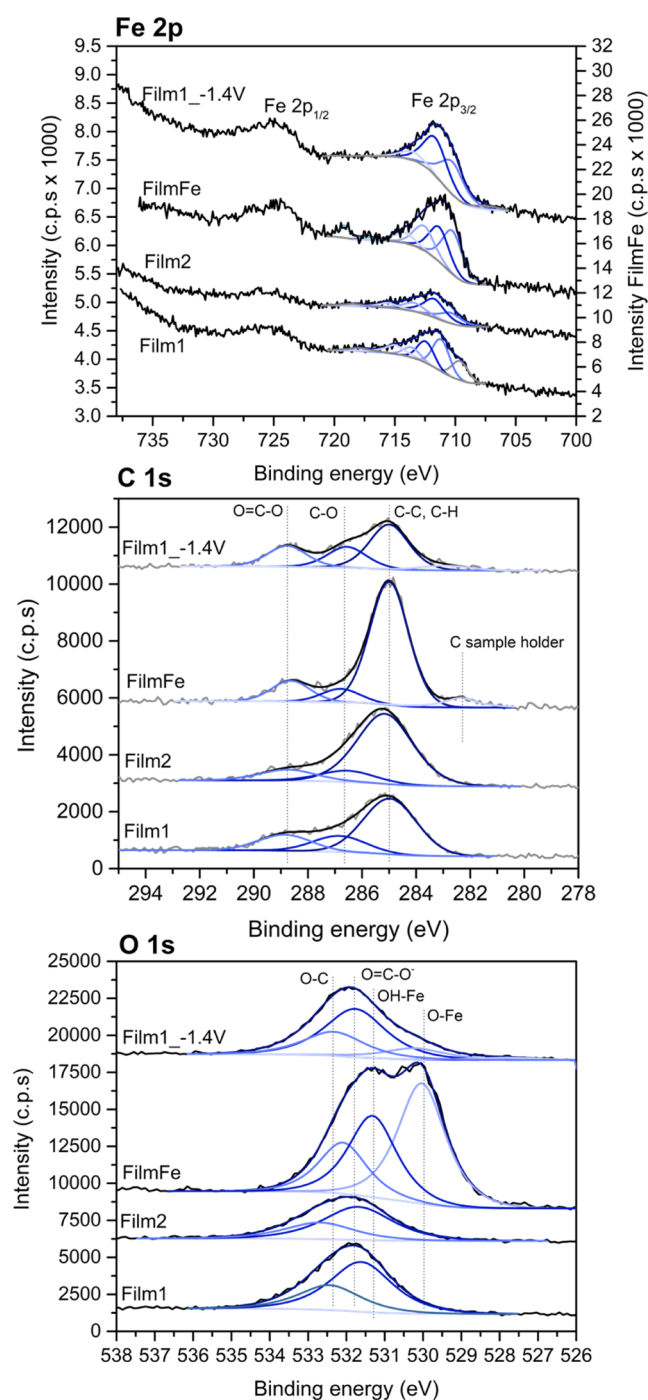


**Figure 7.** XPS regions Fe 2p, C 1s, and O 1s for **Film1**, **Film2**, **FilmFe** (all three films were deposited at  $-1.3$  V), and **Film1**  $-1.4$  V, from bottom to top.

glass substrate, whereas this was not possible for **Film1** as it is much thicker than **Film2**. Moreover, the amount of Fe in **Film1** generally decreases in-depth, which is suggestive of a prelayer of iron oxides/hydroxides. The same was not observed for **Film2**. In fact, the difference between the concentrations of iron at the surface for **Film2** is almost zero. To clarify if there is deposition of the proligand at the electrode surface, a solution without the **M** was used for an attempt of deposition using the same conditions previously used for **Film2**; no film was obtained. In **Tables S3** and **S4**, the Fe/O and Fe/C ratios for both films are shown.

**Analysis of the Growth with Deposition Time with Atomic Force Microscopy.** The morphology of **Film1** was studied over different deposition times to conclude about the film organization and morphology along the different deposition stages. These were deposited with a growth potential of  $-1.3$  V vs Ag/AgCl (3 M NaCl) with deposition times ranging from 8 s to 45 min, over FTO substrates (**Figure S9**).

The FTO electrode (**Figure S10**), as well as the films deposited for 8 and 20 s and 15, 20, and 30 min, was characterized by AFM, obtaining both 2D and 3D images (**Figures S11–S15**). Although AFM did not characterize the film crystallinity, it revealed morphological information and approximate values of film depth. The AFM images of FTO showed a rough material with a morphology characteristic of metal oxides. The images of the 8 and 20 s films show a very ordered morphology, with a dune-like consistency at 8 s, that formed terraces at 20 s (**Figure 10**). The morphologies of the 15, 20, and 30 min films agree with the SEM images of the 1 h films. Herein, it was also noted that the films were constituted by disc-shaped aggregates stacked on the top of each other. Moreover, the AFM image of the 30 min film presents a different layer depositing on top of the stacked aggregates, which could be due to an unorganized growth. This new layer could be further analyzed by the 45 min or 1 h films; however, they were too thick to be characterized by AFM.

The approximate thickness of the 8 and 20 s films was obtained by taking cross-sections from topographical images, reaching values of at least 15 and 185 nm, respectively (**Figure S16**). These shorter deposition approaches could be advantageous if the films were proven to be crystalline by XRD. On the other hand, this fast rate could be associated with random growth and be one of the causes of obtaining an amorphous **Film1** film. For comparison, the **FilmFe** was also analyzed by AFM (**Figure S17**). The images showed a typical metal oxide morphology, similar to that of FTO, as already expected. This agrees with the presence of an iron oxide/hydroxide film.

**Studies for the Evaluation of the Electrochemical and Voltammetric Behavior.** The new films formed are electrochemically active due to the presence of iron metal centers. Therefore, their electrochemical behavior was investigated in a DMF solution. For **Film1**, one pair of redox waves ( $E_p^{ox} = -0.16$  V and  $E_p^{red} = -0.34$  V) is detected and may be attributed to the  $Fe^{3+}/Fe^{2+}$  couple. Similar redox processes are observed for **Film2** (**Figure 11**). In addition, the films are stable, as no current loss is observed after several cycles. The oxidation and reduction peak currents were plotted as a function of the scan rate for **Film1** (**Figure S18**), and the proportional relationship shows that the electrode processes are adsorption controlled. However, when the same graphs were plotted for **Film2**, the reduction peak current density did not show a proportional relationship (**Figure S19a** and **S19b**). As no loss of material from the electrode surface is observed by performing several potential cycles with the film (**Figure 11**), the absence of a proportional relationship is attributed to electron-transfer constraints within the film. However, when the film is grown at a lower potential ( $-1.2$  V) a linear relationship is observed (**Figure S19c** and **S19d**) showing adsorption-controlled processes without the constraints previously discussed. We can state that the linker affects the film properties.

The electroactive surface coverage ( $\Gamma_e$ , nmol  $cm^{-2}$ ) was estimated for both **Film1** and **Film2** based on the integrated

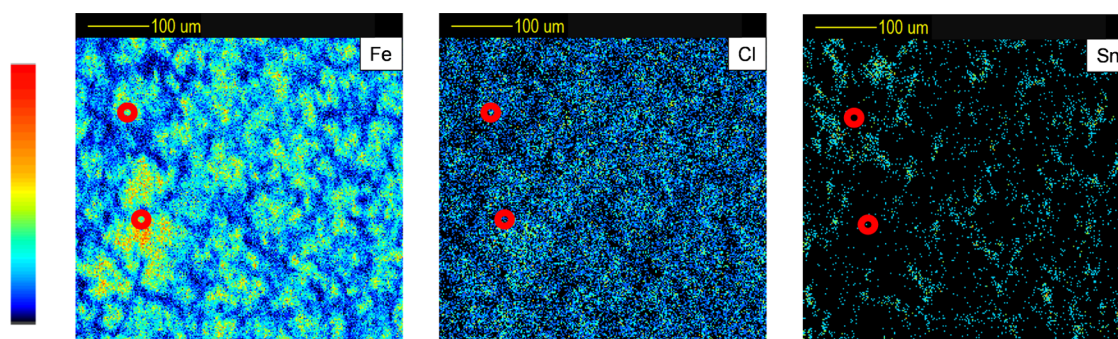


**Figure 8.** Fe, Cl, and Sn 2D elemental distribution of **Film1** (grown at  $-1.3$  V) obtained by PIXE and RBS spectra (circles indicate the location of the analyses performed).

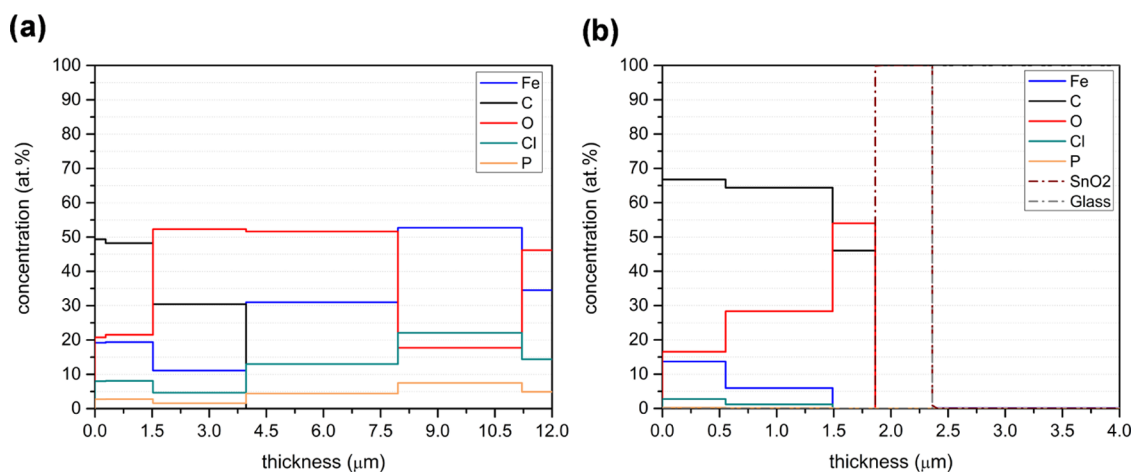


**Figure 9.** Elemental depth profile of (a) **Film1** and (b) **Film2** (both films grown at  $-1.3$  V).

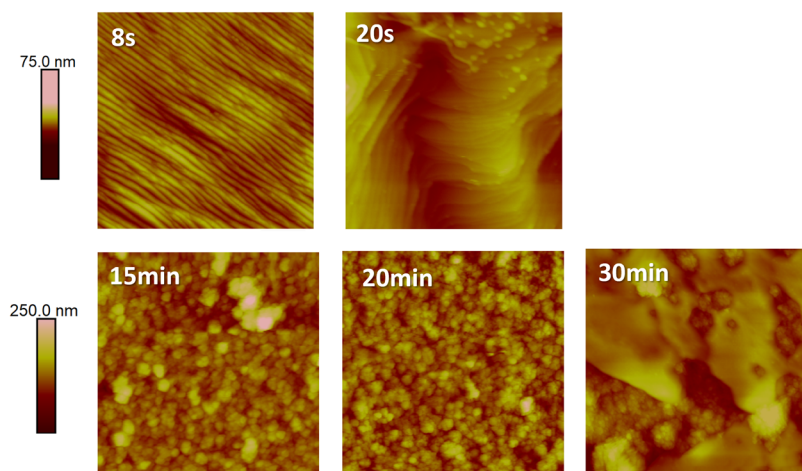


**Figure 10.** 2D AFM images of deposited **Film1** (2:1:1 ratio of **M:DOBDC:PB**, respectively) deposited for 8 and 20 s ( $1 \times 1 \mu\text{m}$ ) and 15, 20, and 30 min ( $2 \times 2 \mu\text{m}$ ).

charges of the  $\text{Fe}^{3+}/\text{Fe}^{2+}$  redox process, and the values obtained were 7.8 for **Film1** and 2.2 for **Film2**.

The voltammetric behavior using ferrocene as a probe of the films was also investigated, and a linear relationship between peak currents and the square root of the scan rate,  $\nu^{1/2}$ , confirms a diffusion-controlled process for **Film1** and **Film2** (Figure S20). As the films are not dense and the FTO is also exposed, the FTO (Figure S20) voltammetric behavior was investigated and compared with the films. It is possible to observe that the voltammetric response exhibited by both films

can be attributed to the exposed FTO surface. In the case of the less dense **Film1**, the redox behavior of Ferrocene closely resembles that of the FTO surface, whereas **Film2**, which is denser (as evident in SEM images), results in a reduced current observed during the Ferrocene redox processes.

## CONCLUSIONS

We have succeeded in synthesizing new iron-organic-based films from two organic proligands of different lengths by the cathodic deposition method, which is milder and finer-tunable.

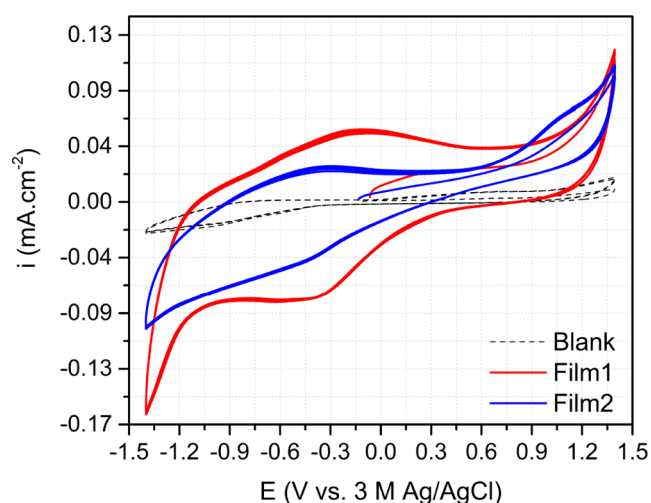


**Figure 11.** Redox behavior of Film1 and Film2 (electrodeposited at  $-1.3$  V) in  $0.1$  M TBAPF<sub>6</sub>/DMF solutions at  $100$  mV s<sup>-1</sup>. Six cycles.

CV studies optimized deposition potentials in the range  $-1.2$  to  $-1.4$  V. Results of XPS analysis indicate that the application of more negative potentials leads to the formation of a prelayer of iron oxide/hydroxide. IR confirmed the coordination of carboxylate to iron centers, with deprotonation of phenol groups taking place upon electrodeposition, resulting in films that were nearly amorphous and with a grain size of ca.  $1$  nm as identified by GISAXS. SEM images showed plate-like aggregates with nonhomogeneous dispersion. XPS confirmed the film composition and deprotonation of the phenol and carboxylic groups. Further, in-depth characterization using PIXE and RBS demonstrated heterogeneity in the films and variable thicknesses based on the prolignand. The elements expected (Fe, O, and C) with different concentrations through the thickness of the film and an iron prelayer were successfully identified at  $-1.3$  V using the longer organic linker. Finally, the stability of the films was electrochemically verified over six cycles in DMF, and one of the films exhibited relatively good voltammetric behavior with a Ferrocene probe, indicating that the prolignand length affects the redox properties. Therefore, this study opens a way to investigate different electrosynthesis conditions, such as metal ions, deposition time, solvent, and mechanisms of linker deprotonation, for the acquisition of new metal–organic materials. Attempts with other metal ions are in progress. The electrocatalytic activity toward CO<sub>2</sub> of these films will be investigated.

## ■ ASSOCIATED CONTENT

### SI Supporting Information

The Supporting Information is available free of charge at <https://pubs.acs.org/doi/10.1021/acs.jpcc.4c02651>.

Additional cyclic voltammograms, IR spectra, SEM images, AFM images, PIXE, and RBS spectra. Chronoamperograms for film growth at different times. XPS and RBS atomic ratios results. Current–potential relationships for the films' redox and voltammetric behavior (PDF)

## ■ AUTHOR INFORMATION

### Corresponding Author

Sara Realista – Centro de Química Estrutural, Institute of Molecular Sciences, Departamento de Química e Bioquímica,

Faculdade de Ciências, Universidade de Lisboa, 1749-016 Lisboa, Portugal; [orcid.org/0000-0003-1066-1200](https://orcid.org/0000-0003-1066-1200); Email: [smrealista@ciencias.ulisboa.pt](mailto:smrealista@ciencias.ulisboa.pt)

## Authors

Ana R. Reis – Centro de Química Estrutural, Institute of Molecular Sciences, Departamento de Química e Bioquímica, Faculdade de Ciências, Universidade de Lisboa, 1749-016 Lisboa, Portugal

Duarte Borralho – Centro de Química Estrutural, Institute of Molecular Sciences, Departamento de Química e Bioquímica, Faculdade de Ciências, Universidade de Lisboa, 1749-016 Lisboa, Portugal

Victoria Corregidor – C2TN, DECN, E.N.10 (km 139.7), Instituto Superior Técnico, Universidade de Lisboa, 2695-066 Bobadela, Portugal

Luís C. Alves – C2TN, DECN, E.N.10 (km 139.7), Instituto Superior Técnico, Universidade de Lisboa, 2695-066 Bobadela, Portugal; [orcid.org/0000-0001-5369-5019](https://orcid.org/0000-0001-5369-5019)

Sérgio Magalhães – IPFN, Instituto de Plasmas e Fusão Nuclear, Campus Tecnológico e Nuclear, Instituto Superior Técnico, Universidade de Lisboa, 2695-066 Bobadela LRS, Portugal; [orcid.org/0000-0002-5858-549X](https://orcid.org/0000-0002-5858-549X)

Telmo Nunes – FCUL Microscopy Facility, Faculdade de Ciências, Universidade de Lisboa, 1749-016 Lisboa, Portugal

Ana S. Viana – Centro de Química Estrutural, Institute of Molecular Sciences, Departamento de Química e Bioquímica, Faculdade de Ciências, Universidade de Lisboa, 1749-016 Lisboa, Portugal

João Pires – Centro de Química Estrutural, Institute of Molecular Sciences, Departamento de Química e Bioquímica, Faculdade de Ciências, Universidade de Lisboa, 1749-016 Lisboa, Portugal; [orcid.org/0000-0002-8374-558X](https://orcid.org/0000-0002-8374-558X)

Ana M. Ferraria – BSIRG, iBB - Institute for Bioengineering and Biosciences, Associate Laboratory i4HB - Institute for Health and Bioeconomy, and Chemical Engineering Department at Instituto Superior Técnico, Universidade de Lisboa, 1049-001 Lisbon, Portugal; [orcid.org/0000-0002-6784-6540](https://orcid.org/0000-0002-6784-6540)

Ana M. Botelho do Rego – BSIRG, iBB - Institute for Bioengineering and Biosciences, Associate Laboratory i4HB - Institute for Health and Bioeconomy, and Chemical Engineering Department at Instituto Superior Técnico, Universidade de Lisboa, 1049-001 Lisbon, Portugal

Paulo N. Martinho – Centro de Química Estrutural, Institute of Molecular Sciences, Departamento de Química e Bioquímica, Faculdade de Ciências, Universidade de Lisboa, 1749-016 Lisboa, Portugal; [orcid.org/0000-0003-2552-6263](https://orcid.org/0000-0003-2552-6263)

Complete contact information is available at: <https://pubs.acs.org/doi/10.1021/acs.jpcc.4c02651>

## Author Contributions

#A.R.R. shares the first authorship with S.R.

## Notes

The authors declare no competing financial interest.

## ■ ACKNOWLEDGMENTS

Centro de Química Estrutural (CQE), Institute of Molecular Sciences (IMS), iBB and i4HB acknowledge the financial support of Fundação para a Ciência e Tecnologia (Projects UIDB/00100/2020: <https://doi.org/10.54499/UIDB/00100/>

2020, UIDP/00100/2020: <https://doi.org/10.54499/UIDP/00100/2020>, LA/P/0056/2020: <https://doi.org/10.54499/LA/P/0056/2020>, UIDB/04565/2020: <https://doi.org/10.54499/UIDB/04565/2020>, UIDP/04565/2020: <https://doi.org/10.54499/UIDP/04565/2020>, LA/P/0140/2020: <https://doi.org/10.54499/LA/P/0140/2020>, and PTDC/QUI-QIN/0252/2021: <https://doi.org/10.54499/PTDC/QUI-QIN/0252/2021>. The NMR spectrometers are part of the National NMR Network (PTNMR) and are partially supported by Infrastructure Project No. 022161 (cofinanced by FEDER through COMPETE 2020, POCI and PORL and FCT through PIDDAC). S.R. and P.N.M. acknowledge FCT for financial support (2020.02134.CEECIND: <https://doi.org/10.54499/2020.02134.CEECIND/CP1605/CT0002> and CEECIND/00509/2017: <https://doi.org/10.54499/CEECIND/00509/2017/CP1387/CT0029>). V.C. and L.C.A. acknowledge FCT for UIDB/04349/2020 project: <https://doi.org/10.54499/UIDB/04349/2020>. We are thankful to the FCUL microscopy facility for the SEM analysis.

## REFERENCES

- (1) Ma, T.; Zhang, J.; Zhang, L.; Zhang, Q.; Xu, X.; Xiong, Y.; Ying, Y.; Fu, Y. Recent Advances in Determination Applications of Emerging Films Based on Nanomaterials. *Adv. Colloid Interface Sci.* **2023**, *311*, No. 102828.
- (2) Jiang, P.; Ji, Z.; Wang, X.; Zhou, F. Surface Functionalization-a New Functional Dimension Added to 3D Printing. *J. Mater. Chem. C* **2020**, *8*, 12380.
- (3) Ruzybayev, I.; Ceylan, A.; Rumaiz, A. K.; Shah, S. I. *Thin Films, Film Formation Techniques*; John Wiley & Sons, Ltd, 2020.
- (4) Martin, P. M. *Handbook of Deposition Technologies for Films and Coatings*, **2010**.
- (5) Glynn, C.; O'Dwyer, C. Solution Processable Metal Oxide Thin Film Deposition and Material Growth for Electronic and Photonic Devices. *Adv. Mater. Interfaces* **2017**, *4*, No. 1600610.
- (6) Ahmed, S. R.; Kim, J.; Tran, V. T.; Suzuki, T.; Neethirajan, S.; Lee, J.; Park, E. Y. In Situ Self-Assembly of Gold Nanoparticles on Hydrophilic and Hydrophobic Substrates for Influenza Virus-Sensing Platform. *Sci. Rep.* **2017**, *7* (1), No. 44495.
- (7) Gaviria, J.; Alcudia, A.; Begines, B.; Beltrán, A. M.; Villarraga, J.; Moriche, R.; Rodríguez-Ortiz, J. A.; Torres, Y. Synthesis and Deposition of Silver Nanoparticles on Porous Titanium Substrates for Biomedical Applications. *Surf. Coat. Technol.* **2021**, *406*, No. 126667.
- (8) Žigon, J.; Kariž, M.; Pavlič, M. Surface Finishing of 3D-Printed Polymers with Selected Coatings. *Polymers* **2020**, *12* (12), No. 2797.
- (9) Noh, J.; Jeong, S.; Lee, J. Y. Ultrafast Formation of Air-Processable and High-Quality Polymer Films on an Aqueous Substrate. *Nat. Commun.* **2016**, *7* (1), No. 12374.
- (10) Guo, Y.; Zou, Y.; Cheng, C.; Wang, L.; Made, R. I.; Goei, R.; Tan, K. W.; Li, S.; Tok, A. I. Y. Noble Metal Alloy Thin Films by Atomic Layer Deposition and Rapid Joule Heating. *Sci. Rep.* **2022**, *12* (1), No. 2522.
- (11) Zhang, Y.; Chang, C. H. Metal-Organic Framework Thin Films: Fabrication, Modification, and Patterning. *Processes* **2020**, *8* (3), No. 377.
- (12) Zhang, Z.; Liu, C.; Zhang, H.; Xu, Z. K.; Ju, F.; Yu, C.; Xu, Y. Ultrafast Interfacial Self-Assembly toward Supramolecular Metal-Organic Films for Water Desalination. *Adv. Sci.* **2022**, *9* (24), No. 2201624.
- (13) Perry, J. J.; Perman, J. A.; Zaworotko, M. J. Design and Synthesis of Metal-Organic Frameworks Using Metal-Organic Polyhedra as Supermolecular Building Blocks. *Chem. Soc. Rev.* **2009**, *38* (5), 1400–1417.
- (14) Kitagawa, S.; Kondo, M. Functional Micropore Chemistry of Crystalline Metal Complex-Assembled Compounds. *Bull. Chem. Soc. Jpn.* **1998**, *71* (8), 1739–1753.
- (15) Yaghi, O. M.; Li, H. Hydrothermal Synthesis of a Metal-Organic Framework Containing Large Rectangular Channels. *J. Am. Chem. Soc.* **1995**, *117* (41), 10401–10402.
- (16) Lin, Z.; Richardson, J. J.; Zhou, J.; Caruso, F. Direct Synthesis of Amorphous Coordination Polymers and Metal-Organic Frameworks. *Nat. Rev. Chem.* **2023**, *7*, 273.
- (17) Bennett, T. D.; Horike, S. Liquid, Glass and Amorphous Solid States of Coordination Polymers and Metal-Organic Frameworks. *Nat. Rev. Mater.* **2018**, *3* (11), 431–440.
- (18) Rayner, J. H.; Powell, H. M. 67. Structure of Molecular Compounds. Part X. Crystal Structure of the Compound of Benzene with an Ammonia-Nickel Cyanide Complex. *J. Chem. Soc.* **1952**, *0*, 319–328.
- (19) Ariga, K.; Leong, D. T.; Mori, T. Nanoarchitectonics for Hybrid and Related Materials for Bio-Oriented Applications. *Adv. Funct. Mater.* **2018**, *28* (27), No. 1702905.
- (20) Rubio-Giménez, V.; Galbiati, M.; Castells-Gil, J.; Almora-Barrios, N.; Navarro-Sánchez, J.; Escorcía-Ariza, G.; Mattera, M.; Arnold, T.; Rawle, J.; Tatay, S.; et al. Bottom-Up Fabrication of Semiconductive Metal-Organic Framework Ultrathin Films. *Adv. Mater.* **2018**, *30* (10), No. 1704291.
- (21) Komiyama, M.; Yoshimoto, K.; Sisido, M.; Ariga, K. Chemistry Can Make Strict and Fuzzy Controls for Bio-Systems: DNA Nanoarchitectonics and Cell-Macromolecular Nanoarchitectonics. *Bull. Chem. Soc. Jpn.* **2017**, *90* (9), 967–1004.
- (22) Sakamoto, R. Bottom-up Creation of Functional Low-Dimensional Materials Based on Metal Complexes. *Bull. Chem. Soc. Jpn.* **2017**, *90* (3), 272–278.
- (23) Li, Z.-Y.; Dai, J.-W.; Damjanovic, M.; akuya Shiga, T.; Wang, J.-H.; Zhao, J.; Oshio, H.; asahiro Yamashita, M.; Bu, X.-H.; Li, Z. Y.; et al. Structure Switching and Modulation of the Magnetic Properties in Diarylethene-Bridged Metallosupramolecular Compounds by Controlled Coordination-Driven Self-Assembly. *Angew. Chem., Int. Ed.* **2019**, *58* (13), 4339–4344.
- (24) Dzhardimalieva, G. I.; Uflyand, I. E. Design and Synthesis of Coordination Polymers with Chelated Units and Their Application in Nanomaterials Science. *RSC Adv.* **2017**, *7* (67), 42242–42288.
- (25) Al-Kutubi, H.; Gascon, J.; Sudhölter, E. J. R.; Rassaei, L. Electrosynthesis of Metal-Organic Frameworks: Challenges and Opportunities. *ChemElectroChem* **2015**, *2* (4), 462–474.
- (26) Sun, L.; Hendon, C. H.; Park, S. S.; Tulchinsky, Y.; Wan, R.; Wang, F.; Walsh, A.; Dincă, M. Is Iron Unique in Promoting Electrical Conductivity in MOFs? *Chem. Sci.* **2017**, *8* (6), 4450–4457.
- (27) Grunder, S.; Valente, C.; Whalley, A. C.; Sampath, S.; Portmann, J.; Botros, Y. Y.; Stoddart, J. F. Molecular Gauge Blocks for Building on the Nanoscale. *Chem. - Eur. J.* **2012**, *18* (49), 15632–15649.
- (28) Armarego, W. L. F.; Perrin, D. D. *Purification of Laboratory Chemicals*; Butterworth Heinemann, 1997.
- (29) Alves, L. C.; Breese, M. B. H.; Alves, E.; Paúl, A.; Da Silva, M. R.; Da Silva, M. F.; Soares, J. C. Micron-Scale Analysis of SiC/SiCf Composites Using the New Lisbon Nuclear Microprobe. *Nucl. Instrum. Methods Phys. Res. Sect. B Beam Interact. Mater. Atoms* **2000**, *161–163*, 334–338.
- (30) Campbell, J. L.; Cureatz, D. J. T.; Flannigan, E. L.; Heirwegh, C. M.; Maxwell, J. A.; Russell, J. L.; Taylor, S. M. The Guelph PIXE Software Package V. *Nucl. Instrum. Methods Phys. Res. Sect. B Beam Interact. Mater. Atoms* **2021**, *499*, 77–88.
- (31) Barradas, N. P.; Jeynes, C. Advanced Physics and Algorithms in the IBA DataFurnace. *Nucl. Instrum. Methods Phys. Res. Sect. B Beam Interact. Mater. Atoms* **2008**, *266* (8), 1875–1879.
- (32) Gurbich, A. *SigmaCalc 1.6*. <http://www-nds.iaea.org>.
- (33) Barradas, N. P.; Alves, E.; Pereira, S.; Shvartsman, V. V.; Kholkin, A. L.; Pereira, E.; O'Donnell, K. P.; Liu, C.; Deatcher, C. J.; Watson, I. M.; Mayer, M. Roughness in GaN/InGaN Films and Multilayers Determined with Rutherford Backscattering. *Nucl. Instrum. Methods Phys. Res. Sect. B Beam Interact. Mater. Atoms* **2004**, *217* (3), 479–497.

- (34) Li, M.; Dincă, M. Reductive Electrosynthesis of Crystalline Metal–Organic Frameworks. *J. Am. Chem. Soc.* **2011**, *133* (33), 12926–12929.
- (35) Zhang, B.; Huang, P.; Chen, J.; Dang, X.; Hu, Y.; Ai, Y.; Zheng, D.; Chen, H. One-Step Controlled Electrodeposition of Iron-Based Binary Metal Organic Nanocomposite. *Appl. Surf. Sci.* **2020**, *504*, No. 144504.
- (36) Li, M.; Dincă, M. Selective Formation of Biphasic Thin Films of Metal–Organic Frameworks by Potential-Controlled Cathodic Electrodeposition. *Chem. Sci.* **2014**, *5* (1), 107–111.
- (37) Rosnes, M. H.; Mathieson, J. S.; Törnroos, K. W.; Johnsen, R. E.; Cronin, L.; Dietzel, P. D. C. Electrospray Mass Spectrometry Investigation into the Formation of CPO-27. *Cryst. Growth Des.* **2019**, *19* (4), 2089–2096.
- (38) Cheansirisomboon, A.; Salinas-Uber, J.; Massera, C.; Roubeau, O.; Youngme, S.; Gamez, P. One-Pot Multiple Metal–Organic Framework Formation: Concomitant Generation of Structural Isomers or of Drastically Distinct Materials. *Eur. J. Inorg. Chem.* **2014**, *2014* (26), 4385–4393.
- (39) Anderson, S. L.; Gładysiak, A.; Boyd, P. G.; Ireland, C. P.; Miéville, P.; Tiana, D.; Vlasisavljevich, B.; Schouwink, P.; Van Beek, W.; Gagnon, K. J.; et al. Formation Pathways of Metal–Organic Frameworks Proceeding through Partial Dissolution of the Metastable Phase. *CrystEngComm* **2017**, *19* (25), 3407–3413.
- (40) Du Bois, D. R.; Wright, K. R.; Bellas, M. K.; Wiesner, N.; Matzger, A. J. Linker Deprotonation and Structural Evolution on the Pathway to MOF-74. *Inorg. Chem.* **2022**, *61* (11), 4550–4554.
- (41) Garzón-Tovar, L.; Carné-Sánchez, A.; Carbonell, C.; Imaz, I.; Maspoch, D. Optimised Room Temperature, Water-Based Synthesis of CPO-27-M Metal-Organic Frameworks with High Space-Time Yields. *J. Mater. Chem. A* **2015**, *3*, 20819.
- (42) Levine, J. R.; Cohen, J. B.; Chung, Y. W.; Georgopoulos, P. Grazing-Incidence Small-Angle X-Ray Scattering: New Tool for Studying Thin Film Growth. *J. Appl. Crystallogr.* **1989**, *22* (6), 528–532.
- (43) Beamson, G.; Briggs, D. *High Resolution XPS of Organic Polymers, the Scienta ESCA300 Database*; Wiley: Chichester, 1992.
- (44) Pletincx, S.; Trotochaud, L.; Fockaert, L. L.; Mol, J. M. C.; Head, A. R.; Karslıoğlu, O.; Bluhm, H.; Terryn, H.; Hauffman, T. In Situ Characterization of the Initial Effect of Water on Molecular Interactions at the Interface of Organic/Inorganic Hybrid Systems. *Sci. Rep.* **2017**, *7* (1), No. 45123.